Potassium-Ion Battery Electrodes from Potassium Ferricyanide Nanoplatelets: Thin Platelets and Thick Electrodes Unlock High Areal Capacity and Excellent Rate Performance

Harneet Kaur, Bharathi Konkena, Mark McCrystall, Kevin Synnatschke, Cian Gabbett, Jose Munuera, Jack Maughan, Lee Gannon, Ross Smith, Yumei Jiang, Tian Carey, Cormac Mc Guinness, Valeria Nicolosi, and Jonathan N Coleman**

Recent efforts to develop cathode materials for potassium-ion batteries (KIBs) have focused on maximizing specific capacity. However, real applications will require thick electrodes with high areal capacity that can achieve reasonable rate performance, which is a significant challenge. While Prussian blue analogs (PBAs) show promise for fast K-ion storage, they often require bespoke synthesis. In this study, potassium ferricyanide ($K_3Fe(CN)_6$, KFC) is explored as a commercially available and cost-effective alternative. Using liquid-phase exfoliation, KFC powder is converted into 2D nanoplatelets, which are combined with single wall carbon nanotubes (SWCNT) to form porous, conductive, and mechanically tough electrodes. This KFC/SWCNT nanocomposite delivers reversible capacities up to 98 mAh g^{-1} at 20 mA g^{-1}, with 92% capacity retention after 500 cycles. These composite electrodes can be fabricated with thicknesses and areal mass loadings up to 105 µm and 9.6 mg cm^{-2} respectively and achieve an areal capacity of 0.65 mAh cm^{-2} at 20 mA g^{-1}, the highest reported among PBAs. Despite being limited by solid-state diffusion, the short diffusion paths associate with the nanoplatelet geometry enable excellent rate performance.

1. Introduction

Lithium-ion (Li-ion) batteries, despite their widespread use,[1] are increasingly predicted to face sustainability challenges due to the limited abundance and uneven geographical distribution of lithium resources.[2] This has led to a growing interest in finding alternative battery technologies. Among the most promising alternatives are sodium-ion (Na-ion) and potassium-ion (K-ion) batteries, which leverage the abundance of sodium (Na) and potassium (K).[3] In the past decade, Na-ion batteries have already begun to be commercialized by several companies, demonstrating their potential as a viable replacement for Li-ion technology.[4] In contrast, K-ion battery technology remains largely at the lab stage.

However, K-ion batteries are a compelling alternative,[5] sharing many advantages with Na-ion batteries,[6] including low cost and the ability to use cheaper aluminum instead of copper as a current collector, due to potassium's non-alloying nature with aluminum.[3b,7] They also offer additional benefits; for instance, the standard redox potential for K^+/K (−2.93 V vs standard hydrogen electrode, SHE) is more negative than that of Na^+/Na (−2.71 V vs SHE), facilitating higher energy densities.[7] Additionally, graphite, a common anode material used in lithium-ion batteries but not in Na-ion batteries, can be used in K-ion batteries (theoretical capacity of 279 mAh g^{-1}),[8] allowing for the adaptation of existing graphite anode technology from Li-ion to K-ion batteries.[8b] Despite potassium's inherent reactivity compared to lithium and sodium, recent advancements have mitigated safety concerns, particularly through the alloying of anodes with Na/K.[9]

However, significant challenges remain in the development of suitable cathode materials for K-ion batteries.[10] Among the most studied materials in recent years are Prussian blue and its analogs (PBAs).[11] This set of materials has garnered attention due to their unique open crystalline frameworks, that feature

H. Kaur, B. Konkena, M. McCrystall, K. Synnatschke, C. Gabbett, J. Munuera, J. Maughan, L. Gannon, R. Smith, Y. Jiang, T. Carey, C. M. Guinness, J. N Coleman
School of Physics
CRANN and AMBER Research Centers
Trinity College Dublin
Dublin 2 D02 E8C0, Ireland
E-mail: konkenab@tcd.ie; colemaj@tcd.ie
V. Nicolosi
School of Chemistry
CRANN and AMBER Research Centers
Trinity College Dublin
Dublin 2 D02W9K7, Ireland

The ORCID identification number(s) for the author(s) of this article can be found under https://doi.org/10.1002/aenm.202500488

DOI: 10.1002/aenm.202500488

large interstitial sites and 3D channels, potentially facilitating fast ion flow. However, the synthesis of PBAs is not straightforward and often involves complex multi-step synthesis procedures.[12]

However, once synthesized, PBAs demonstrate excellent properties as cathode materials, such as good discharge capacity (up to 150 mAh g^{-1}, see Table S2, Supporting Information), rate capability, and long cyclic performance.[11] However, their practical application is hindered by the fact that most studies have focused on relatively thin electrodes, with thickness generally far below 50 μm. This is a problem as commercial electrodes need to be thick to achieve high areal capacity. To date, there is only one reported study where a PBA electrode, specifically copper hexacyanoferrate (CuHCF), achieved a high mass loading of 10 mg cm^{-2}, equivalent to a thickness of 100 μm, resulting in a high areal capacity of 0.6 mAh cm^{-2}.[13] However, the synthesis method used in this study, a co-precipitation process, is difficult to control and can lead to nanoparticle agglomeration and reduced theoretical capacity due to the presence of zeolitic water.[13] It is also worth noting that the fabrication of thick electrodes requires the availability of reasonably large active masses. This may not be possible for materials fabricated by the user via bespoke synthetic methods that can give low yields.[14]

Given that conventional commercial battery electrodes are typically 100 μm thick,[15] designing thicker electrodes with higher mass loading of active materials is crucial to the development of potassium-ion batteries. Such thick electrodes are needed to maximize areal capacity leading to high energy density.[16] In this paper, we aim to identify a cost-effective, commercially available alternative to PBAs that can be formed into thick, high-performance electrodes. We explore the possibility of using commercially available potassium ferricyanide (KFC) as a potential cathode material for K-ion batteries. Unlike PBAs, KFC is relatively cheap, contains no crystalline water, and has a reasonably high theoretical capacity of 81 mAh g^{-1}.[17] Although KFC (in the form of micro-particles) has been demonstrated as a cathode material for sodium-ion batteries,[17] to date no research has reported on the direct use of commercial KFC in any form as a cathode in K-ion batteries.

In this study, we synthesize 2D-nanoplatelets of KFC through a simple liquid-phase exfoliation technique and integrate these nanoplatelets with conductive single-walled carbon nanotubes (SWCNTs) to create highly conductive, porous, free-standing electrodes at high mass loadings. The resulting nanocomposite electrodes demonstrate a reversible discharge capacity of up to 98 mAh g^{-1} at a low current. Moreover, relatively thick electrodes ($M_T/A \approx 9.6$ mg cm^{-2}, 105 μm thick) displayed a very high areal capacity of 0.65 mAh cm^{-2} @ 20 mA g^{-1} and an excellent capacity retention of 91.5% after 500 cycles.

2. Results and Discussion

2.1. Synthesis and Characterization of 2D-KFC Nanoplatelets

Commercially available $K_3Fe(CN)_6$ powder appears as a vibrant red compound (**Figure 1a**), wherein the central Fe atom is octahedrally coordinated with six CN ligands (Figure S1, Supporting Information). Strong field ligands like CN significantly influence the energy levels of the *d*-orbitals of the central Fe ion within a coordination complex, leading to substantial splitting of the *d*-orbitals.[18] Consequently, a notable energy disparity arises between the $t_{2\ g}$ (higher) and $e_{2\ g}$ (lower) set of *d*-orbitals, resulting in a distorted octahedral geometry.[19] This distortion manifests as varying bond lengths between Fe and CN ligands due to the differential bonding strengths of the ligands.

We speculated that such bonding anisotropy in the compound might facilitate preferential cleavage along certain planes. It is known that materials with bonding anisotropy can be converted into quasi-2D nanoplatelets via a process known as liquid phase exfoliation.[20] Although first developed to exfoliate van der Waals solids, it was recently demonstrated that this method could convert non-van der Waals materials into quasi-2D nanoplatelets so long as some bonding anisotropy is present.[21]

Here, we performed liquid phase exfoliation of bulk KFC (see SEM image in Figure 1b) in anhydrous degassed solvent 2-propanol in an inert atmosphere (see method section for complete details), yielding a yellow-colored dispersion as depicted in Figure 1c. Subsequently, the dispersion was optically characterized using UV–vis absorption spectroscopy. As shown in Figure 1d, the absorption coefficient spectra of the exfoliated dispersion with respect to wavelength exhibit three intense absorption bands centered at 416 nm (I), 303 nm (II), and 260 nm (III). The absorption bands (I and II) at 416 and 303 nm are attributed to charge-transfer transitions from the CN ligand to the $t_{2\ g}$ level of the Fe ion, while the 260 nm (III) band corresponds to charge-transfer transition from the ligand into the $e_{2\ g}$ level. These findings are consistent with the existing literature on KFC in the solution phase.[22]

The exfoliated products were characterized morphologically by transmission electron microscopy (TEM). The TEM images (Figure 1e) depict the quasi-2D morphology of the exfoliation products, with a mean length $\langle L \rangle$ of 140 nm. Energy dispersive X-ray spectroscopy (EDX) conducted on individual randomly selected nanoplatelets is shown in Figure 1f, confirms the presence of C, N, Fe, K, and Cu elements similar to bulk obtained from SEM-EDX (refer to Figure S2, Supporting Information). Notably, oxygen is absent in the elemental EDX scans, confirming that the nanoplatelets formed by inert gas LPE are anhydrous. Although we attempted to obtain information on the atomic structure of the exfoliated material by HRTEM, this proved impossible due to the extreme beam sensitivity of the sample. For the calculation of the average atomic ratio, a free-standing film of exfoliation nanoplatelets was prepared by filtering the dispersion. The film is dried in a vacuum overnight, and subject to scanning electron microscopy (SEM) for EDX measurements at multiple regions (refer to Figure S2, Supporting Information)). Note that stoichiometry, detailed elemental compositions, and mappings of both bulk and 2D-form of KFC were determined using SEM-EDX results (Figures S2,S3, Supporting Information)). The average elemental composition of $\langle K/Fe \rangle = 2.9$ and $\langle N/Fe \rangle = 6.5$, indicating the surface stoichiometry of the nanoplatelets as $K_{2.9}FeC_{5.2}N_{6.5}$ matches well the average elemental composition of bulk, $K_{2.9}FeC_5N_{6.4}$ (Figure S2, Supporting Information). Note that carbon element being the most common contaminant in vacuum chambers, cannot be measured accurately.

The crystalline structure and phase of the KFC nanoplatelets were assessed using powder XRD and Raman spectroscopy and were compared with those of bulk particles. **Figure 2a** illustrates

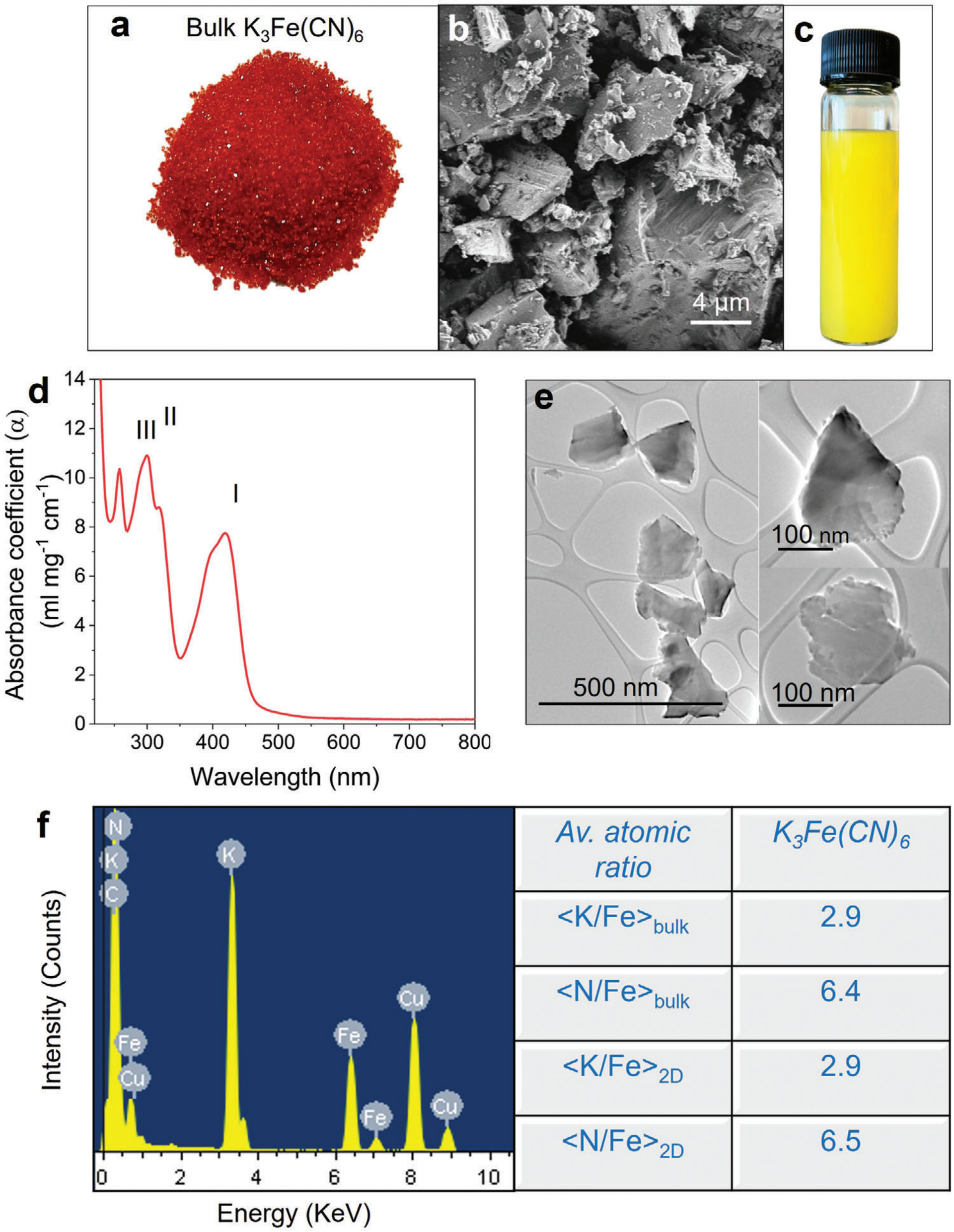

Av. atomic ratio	$K_3Fe(CN)_6$
$\langle K/Fe\rangle_{bulk}$	2.9
$\langle N/Fe\rangle_{bulk}$	6.4
$\langle K/Fe\rangle_{2D}$	2.9
$\langle N/Fe\rangle_{2D}$	6.5

Figure 1. Synthesis of $K_3Fe(CN)_6$ nanoplatelets. a) Commercially available potassium ferricyanide crystals, and its scanning electron microscopy image b) confirm the presence of non-layered 3D-bulk structure. c) Dispersion of $K_3Fe(CN)_6$ in anhydrous 2-propanol, produced by liquid phase exfoliation in inert atmosphere, and d) Absorbance coefficient spectra of 2D-nanoplatelets plotted versus wavelength. e) Transmission electron microscopy images of the exfoliated 2D-nanoplatelets. f) Energy-dispersive X-ray spectra on a single nanoplatelet confirms the presence of C, N, K, and Fe atoms. The Cu signal is originating from the TEM grid. The right table in (f) represents the average atomic ratio of elements in bulk and 2D-nanoplatelets of $K_3Fe(CN)_6$ obtained from SEM-EDX (refer to Supporting Information for the SEM-EDX spectra).

distinct differences in the diffraction spectra of bulk and exfoliated nanoplatelets. The detailed analysis provided in Figure S1 (Supporting Information) reveals that the diffraction pattern from the bulk is indexed to the monoclinic crystal lattice structure, space group: $P2_1c$, whereas that of the nanoplatelets corresponds to the orthorhombic crystal lattice system, space group: *Pnca*.[19] It is established that KFC exists in two crystal lattice forms, monoclinic and orthorhombic (Figure S1, Supporting Information).[19] The observed phase transition from monoclinic to orthorhombic during the LPE process confirms the relaxation of the lattice structure toward higher symmetry. This is also accompanied by changes in the Raman spectrum as shown in Figure 2b, where the lattice phonon mode at 158 cm^{-1} splits compared to the bulk configuration.[23] This splitting results in a new feature at 173 cm^{-1}. The peak at 387 cm^{-1} in the bulk demonstrates a shift to 385 cm^{-1} in 2D platelets, indicating a transition to an orthorhombic structure of higher symmetry.[24] Thus, in the exfoliated KFC sample, the $Fe(CN)_6$ octahedra experiences

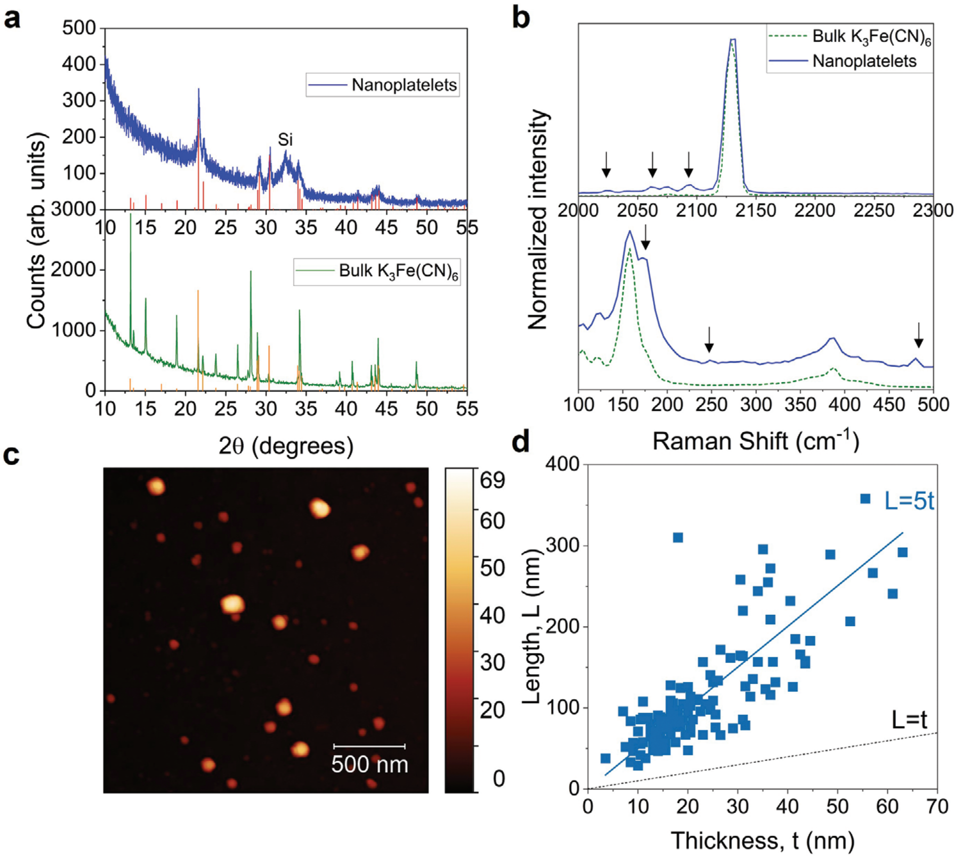

Figure 2. Characterization of $K_3Fe(CN)_6$ nanoplatelets. a) X-ray diffraction spectra of $K_3Fe(CN)_6$ in the form of exfoliated nanoplatelets (top) and bulk powder (bottom). b) Raman spectra of $K_3Fe(CN)_6$ in the form of exfoliated nanoplatelets and bulk powder in both the high- (top) and low-(bottom) with different wavenumber regimes. c) AFM image of $K_3Fe(CN)_6$ nanoplatelets deposited on a Si/SiO_2 substrate. d) Length and thickness of individual nanoplatelets. The solid line represents an aspect ratio (AR = L/t) of 5, where the dotted line represents the results expected for nanoparticles (*L* = *t*).

distortion with a nonlinear Fe–C–N–Fe arrangement,[24] allowing for additional vibrational modes, indicated with arrows. However, the other peaks associated with the CN stretching modes remain unaffected.

Atomic force microscopy was utilized to confirm the 2D nature of the nanoplatelets generated by the LPE process. As shown in Figure 2c,d, the KFC nanoplatelets have lengths (defined as the largest lateral dimension) between 25 and 300 nm and thicknesses between 5 and 60 nm. The mean length and thickness were found to be <L≥116 nm and <t≥22 nm (Figure S4, Supporting Information). It is clear from this data that their lengths are considerably larger than their thicknesses, confirming their nanoplatelet geometry.

However, these KFC nanoplatelets have relatively small aspect ratios, defined by the length-to-thickness ratio, L/t. This aspect ratio provides a measure of the 2D-nature of the nanoplatelets. A straight line fit to the data in Figure 2d reveals an average aspect ratio (AR) of 5, consistent with a quasi-2D-morphology for the LPE-produced KFC nanoplatelets. This aspect-ratio is small compared to the nanosheets produced by LPE of layered materials (AR up to 100).[20a,25] As shown by us and others,[21,26] LPE of non-layered materials can occur due to the presence of directional anisotropy in the inter-atomic bonding strength. Indeed the aspect ratio of exfoliated nanoplatelets is directly related to the degree of bonding anisotropy.[20b,21] As a result, exfoliation of non-layered crystals often results in nanoplatelets with very low aspect ratios (≈4–20).[21,26a,27] Our relatively low aspect ratios stem from the fact that, despite the known variations in bond lengths, interatomic bonding in KFC clearly has relatively low anisotropy, especially compared to layered crystals where the inter-layer interactions are van der Waals in nature.

This work confirms that we have produced KFC nanoplatelets by liquid phase exfoliation of bulk KFC. By analyzing the output of our exfoliation process, we found the nanosheet yield to be 13–15% (ratio of the mass of nanosheets produced to the mass of starting material). In addition, we found the production to be 12 mg h^{-1}/PBAsh for an exfoliation (solvent) volume of 10 ml. We emphasize that this work has been demonstrated only at the lab scale. However, we note that the scaleup of liquid phase exfoliation has previously been demonstrated.[28] Thus, we believe that it should be possible to scale up this process.

2.2. Application of Nanoplatelets as K-Ion Storing Cathodes

A wide range of 2D and quasi-2D materials have proven to be excellent active materials for use in Li-ion, Na-ion, and

K-ion batteries.[26a,29] Here we evaluate the utility of the 2D-nanoplatelets of KFC developed in this study, as active materials in K-ion battery electrodes. Our material demonstrates several advantages over traditional PBAs. First, KFC are commercially available, unlike PBAs which often involve complex multi-step synthesis procedures.[12] Second, KFC synthesis can be scaled up for mass production, something that is challenging for PBAs due to the need for optimization of a complex set of synthesis parameters, such as reaction time, temperature, reactant concentration, and pH.[11,14a]

Moreover, the vast majority of KIB literature using PBAs focuses on thin electrodes (<10 µm thickness)[11] with the aim of maximizing the specific capacity. The unstated assumption is that the electrode thickness can be increased to commercially relevant levels (≈100 µm) while retaining the maximized specific capacity. However, this is often not achievable. Unfortunately, the specific capacity often falls off with increasing electrode thickness, for example, due to problems associated with charge delivery.[30] In addition, due to charge and mass transport limitations,[31] the rate performance depends strongly on electrode thickness[32] and can degrade significantly as electrode thickness is increased toward or beyond 100 µm. Such thickness effects result in lower than-anticipated specific capacity and energy density in thick electrodes. Another generally unappreciated problem is that for some materials mechanical instabilities forbid solution processing of films thicker than the so-called critical crack thickness.[33] Generating thicker electrodes requires increasing the mechanical strength and toughness of the electrode.[16,33a]

Each of these problems can be mitigated by using carbon nanotubes as both binder and conductive additive instead of the usual combination of polymer and carbon black.[16,34] Nanotube addition enhances the electrode conductivity, maximizing charge distribution, and usually leads to near-theoretical capacity at high electrode thickness.[16,35] In addition, increasing electrode conductivity reduces the contribution of the electrode resistance to the factors limiting rate performance,[31,34b] resulting in increased capacity at high rates. Finally, adding nanotubes dramatically increases the mechanical performance of electrodes,[36] allowing the fabrication of very thick, high-performance battery electrodes.[16,34a] Therefore, in this article, we evaluate the fabrication of K-ion battery electrodes from the mixtures of KFC nanoplatelets and single-walled carbon nanotubes. This allows us to produce relatively thick electrodes with near theoretical capacities and excellent rate performance.

The fabrication of nanocomposite cathodes includes incorporating 2D-nanoplatelets of KFC and SWCNTs, involving mixing dispersions of both materials in 2-propanol to achieve a weight ratio of 80% for the active material (2D-nanoplatelets) and 20% for SWCNT (see methods). This mixed dispersion was vacuum-filtered onto the Celgard 2320 membrane, resulting in the formation of free-standing films after peeling from the Celgard substrate (**Figure** 3a). Electrodes of different thicknesses were produced by utilizing various areal mass loadings (the thickness dependence will be discussed in detail below). The total mass loading, which includes both active material (KFC) mass and nanotube mass, is denoted as M_T/A and was in the range 0.38–9.5 mg cm^{-2}. The mass loading of only the active component (KFC) is referred to as M_{Act}/A and was in the range of 0.31–7.6 mg cm^{-2}. The films were sectioned into 0.178 cm^2 areas for electrochemical testing. SEM analysis of the $M_T/A = 0.56$ mg cm^{-2} electrode (thickness ≈7.4 µm) is shown in Figure 3b and reveals a porous, open structure comprising KFC nanoplatelets evenly dispersed within a uniform SWCNT network. Additionally, we have performed XPS measurements on both exfoliated 2D platelets and composite electrodes to give more insights into the structural information, with the results presented in Figures S5,S6 (Supporting Information). The results decisively show that no Fe^{2+} sites are present within the KFC structure, as evidenced by the absence of features at the 708.5 eV binding energy of the Fe^{II} 2p$_{3/2}$ photoelectron line; consequently, it confirms that all iron sites are in the Fe^{+3} oxidation state (Figures S5,S6, Supporting Information).

We first characterized the 2D-KFC/SWCNT composite electrode with $M_T/A = 0.56$ mg cm^{-2} via a series of electrochemical measurements. Initially, we studied their electrochemical K-ion storage properties using galvanostatic charge–discharge cycling at a specific current density of 20 mA g^{-1}. Unless stated otherwise, we calculated the discharge capacity and current density by taking into account the weight of the active material (M_{Act}) and expressing them as Q/M_{Act} and $I/M_{Act,}$ respectively. Our KFC/SWCNT electrodes demonstrate an open circuit potential of 3.2 V. Figure 3c displays the charge–discharge voltage profiles for the first 6 standard activation cycles, allowing the SEI layer to form on the electrode surface. During the first cycle, we didn't observe a plateau in the charge profiles because all the Fe sites in the KFC were in the oxidized state of +3,[37] it has been evidenced by XPS analysis (Figure S5, Supporting Information). The KFC electrode shows a distinct potential plateau at 3.5 V during the charge and at 3.28 V during the discharge due to the oxidation/reduction of the Fe^{III}/Fe^{II} couple. Despite a slight electrochemical polarization in the first cycle, the voltage profiles of the successive scans remained almost unchanged, indicating a very reversible and stable K-ion insertion reaction of the 2D-KFC/SWCNT cathode.

In Figure 3c, the first charge cycle of the GCD curves at 20 mA g^{-1} exhibits a very low initial charge capacity of 10 mAh g^{-1}. When the KFC/SWCNT electrode was charged in the first cycle, K$^+$ ions were extracted from the $K_3Fe(CN)_6$ matrix. This extraction process demands more energy, especially during the forward scan, leading to the extraction of only 10% of the K$^+$ ions from the $K_3Fe(CN)_6$ matrix. This limited extraction is attributed to the higher potential limit of 4 V, which is established to prevent electrolyte decomposition. As a result, only 10% of the theoretical capacity is achieved in the first cycle. However, during the subsequent discharge process, a capacity of 88.7 mAh g^{-1} is observed, due to the competitive insertion of new K$^+$ ions from metallic-K into the KFC matrix. In the second charging cycle, an increase in capacity gain is observed as these newly added K$^+$ ions are actively extracted from the $K_3Fe(CN)_6$ matrix at a potential close to 3.55 V, thus near theoretical capacity is achieved. Therefore, the low initial CE is mainly attributed to the incomplete activation of the electrode material during its chemical or structural adjustments while forming the SEI layer, the irreversible degradation of the electrolyte, and excess K-ion entrapment in the active material.[38] Over the next 5 activation cycles, the charge capacity of the electrode gradually decreased from 88.7 to 81.3 mAh g^{-1}, while the CE rose to 99%, demonstrating stable SEI formation. The CV profiles of the

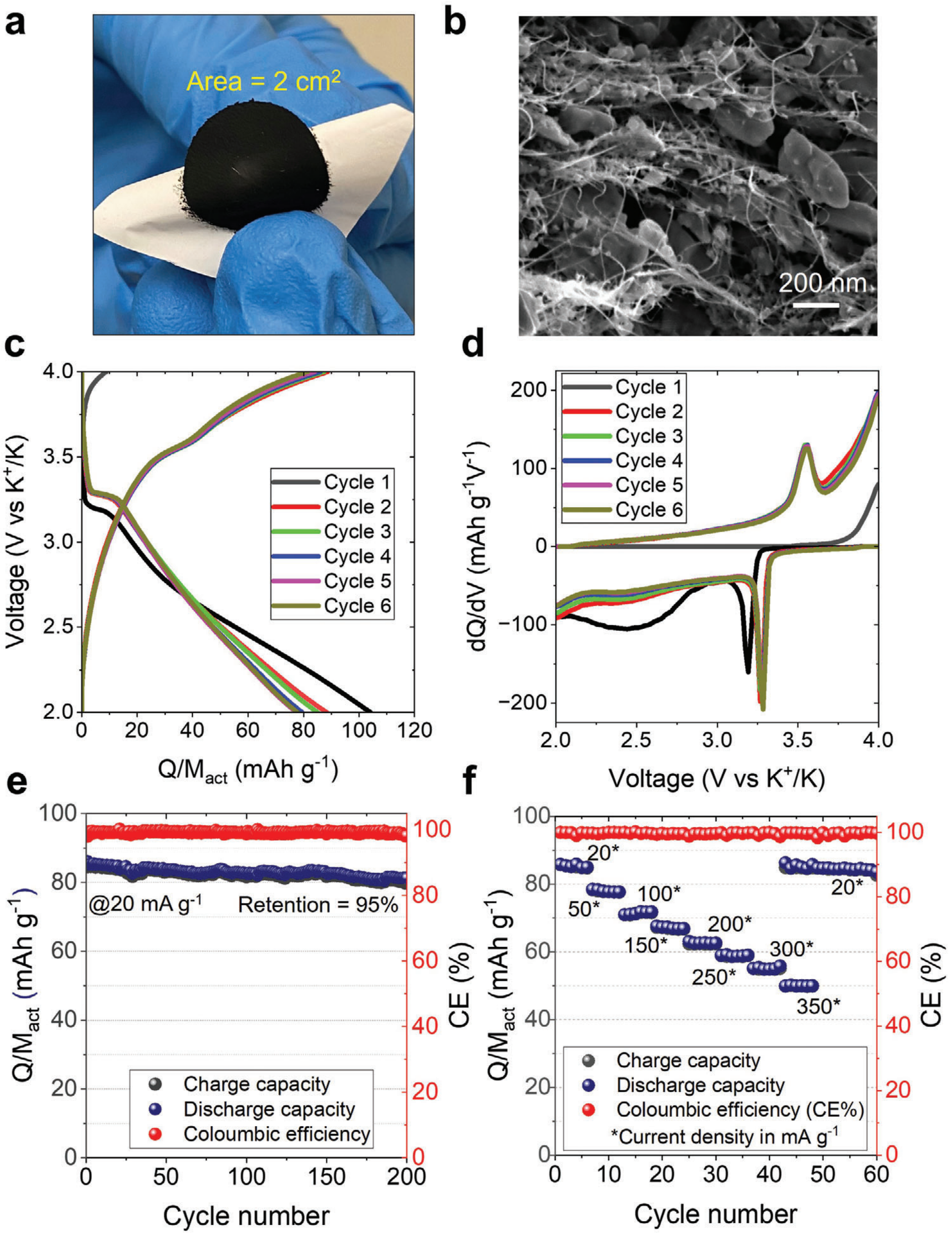

Figure 3. Electrochemical performance of the KFC/SWCNT cells within a 2–4 V (vs K$^+$/K) window. a) A photograph of an electrode consisting of an 80/20 wt/wt mixture of KFC 2D-nanoplatelets and single walled carbon nanotubes (thickness, $L_E = 7.4$ μm). b) SEM close view of the electrode surface. c) The galvanostatic charge–discharge curves (collected at 20 mA g^{-1} for the first six consecutive cycles. d) and the corresponding differential capacity plots e) Specific capacity and Coulombic efficiency measured for 200 cycles at a current density of 20 mA g^{-1}. f) Specific capacity and Coulombic efficiency plotted as a function of cycle number, measured at different current densities as indicated on the panel in units of mA g^{-1}. All speccific capacity values are normalized to active mass and denoted as Q/M_{Act}.

composite electrodes are shown in Figure S7a (Supporting Information). The composite cathodes display one pair of distinct redox peaks at 3.5/3.26 V (vs K$^+$/K), which are attributed to the redox reaction of the [Fe(CN)6]$^{3-/4-}$ couple via a reversible K$^+$ intercalation/deintercalation mechanism, which will be discussed later. When the electrodes are subjected to cyclic voltammetry at a scan rate of 0.1 mV s^{-1}, significant deformation of the CV curves is observed (Figure S7a, Supporting Information). It is known that in battery electrodes, where ion intercalation occurs from a liquid electrolyte to a solid material, local variations in the electrolyte resistance can result in deformation of the CV curves thus complicating qualitative interpretation.[38] Erinmwingbovo et al. have demonstrated that, while differential capacity plots for PB analogs exhibit a similar shape to classical CV curves, they do not overlap due to distinct non-equilibrium conditions in their experiments. Multiple factors contribute to this kinetic behavior, with electrolyte resistance and mass transport within the solid material playing a significant role. To reduce the effects of non-equilibrium conditions during experimentation, plotting differential capacity curves (E vs dQ/dV) rather than cyclic voltammetry curves provides a clearer qualitative analysis, as the peak of these curves indicates the "maximum differential charge" of the material throughout the charge–discharge process.[38a,39,40]

Consequently, we conducted an assessment of the redox chemistry of the KFC cathode with K-ions using differential capacity plots analysis, as depicted in Figure 3d. The initial positive scan does not reveal any oxidation peak, as it was previously demonstrated that the Fe sites in KFC exist in the oxidized state of +3. During the subsequent discharge, the primary feature is observed at 3.18 V, which corresponds to the reduction of Fe^{3+} sites in the KFC cathode to form Fe^{2+}.[17] Additionally, a broad feature is noted at 2.5 V, primarily resulting from extra K-ion adsorption/desorption during the formation of SEI on the KFC/SWCNT electrode surface and the generation of some irreversible intermediates during the first cycle.[41] In the second cycle, the anodic peak is observed at 3.55 V, while the cathodic peak shifts to 3.28 V. This can be attributed to the oxidation/reduction of the $[Fe(CN)_6]^{3-/4-}$ couple, corresponding to the extraction and insertion of K^+ ions from and into the crystal structure of $K_3Fe(CN)_6$.[37,41a,42] The shapes and areas of the peaks remain almost unchanged during the successive scans, conclusively demonstrating a reversible structural and electrochemical stability of the KFC/SWCNT composite electrode for the K-storage reaction.

The potential positions resemble very much the CV features of the $[Fe(CN)_6]^{3-/4-}$ couple in the solid $K_4Fe(CN)_6$ and $Na_4Fe(CN)_6$ electrode.[43] Thus, the redox reaction of $K_3Fe(CN)_6$ as an insoluble solid electrode could be assigned to proceed through a reversible K^+ insertion/extraction mechanism:

$$K_3Fe(CN)_6 + xe^- + xK^+ \rightleftarrows K_{3+x}Fe(CN)_6 \tag{1}$$

Since $K_3Fe(CN)_6$ can accommodate one K^+ ion stoichiometrically to become $K_4Fe(CN)_6$, based on one-electron transfer, the theoretical capacity of $K_3Fe(CN)_6$ is calculated to be 81 mAh g^{-1}.[17]

To study the cycling performance of the KFC/SWCNT nanocomposite electrodes, the composite electrode was subjected to 200 cycles at a current density of 20 mA g^{-1} (following the initial 6 activation cycles, Figure 3e). During cycling, a consistent and robust cycling performance was observed, demonstrating stability with a substantial capacity retention of 95% after 200 cycles with CE exceeding 99%. This indicates the effective reversibility of the electrochemical potassiation/de-potassiation reactions and showcases outstanding cyclic charge–discharge performance with high CE. Further, the electrode durability was tested by subjecting the electrode to 500 cycles at a high current density of 50 mA g^{-1} (Figure S7, Supporting Information). As depicted in Figure S7b (Supporting Information), the charge capacity remained at 79 mAh g^{-1} for the first 250 cycles and gradually decreased to 71 mAh g^{-1} after 500 cycles. This demonstrates an outstanding capacity retention of 90% for this particular electrode. It is essential to evaluate the capacity contribution of carbon nanotubes (CNT). As shown in Figure S7c (Supporting Information), the measured specific capacity of the SWCNTs electrode for K-ion is ≈35 mAh g^{-1} at a current density of 50 mA g^{-1}, therefore, the maximum contribution of SWCNTs in our electrodes having 20 wt.% SWCNTs is 7 mAh g^{-1}, this value is relatively small in comparison to the overall KFC/SWCNT composite electrode capacity (≈75 mAh g^{-1} at 50 mA g^{-1} for this electrode).

The rate performance was evaluated at current densities ranging from 20 to 350 mA g^{-1}, as depicted in Figure 3f. The composite electrodes demonstrated the expected decrease in capacity as the charge–discharge current increases. For example, the observed capacities were 85, 62.6, and 49.9 mAh g^{-1} when the current changed from 20 to 200 to 350 mA g^{-1}, respectively. Upon reverting the current to 20 mA g^{-1}, the electrode recovered the capacity of 84.7 mAh g^{-1}, indicating remarkable stability, with the final capacity reaching 99% of its previous value at 20 mA g^{-1}.

It is important to mention that experiments using 2 м KFSI in TEP electrolyte offer superior performance compared to other electrolytes, such as 0.8 м KPF_6 in EC/DEC (1:1) and 1 м KFSI in EC/DEC (1:1) (refer to Table S1, Figure S8, Supporting Information). KFSI is known for its high ionic conductivity and chemical durability.[44] The consistent cycling performance observed with 2 м KFSI in TEP is likely a result of the development of a strong solid electrolyte interphase (SEI), results are in line with previous findings.[44,45]

2.3. KFC/SWCNT Composites as Very Thick, High Areal Capacity K-Ion Storing Cathodes

The results described above show $K_3Fe(CN)_6$ nanoplatelets to be a very stable cathode material for K-ion storage, albeit one with a low-rate specific capacity ($Q/M_{Act} \approx 85$ mAh g^{-1} @ 20 mA g^{-1}) that is somewhat below the state-of-the art for PBAs which is ≈130 mAh g^{-1} @ 20 mA g^{-1} (see Ref. [46] and Table S2, Supporting Information). However, in real battery electrodes, achieving very high active-mass-normalized capacity (Q/M_{Act}) is not necessarily of primary importance. What is more important from a practical standpoint is achieving high areal capacity (Q/A) as this parameter is a critical determinant of the cell energy density.[16] The areal capacity is given by $Q/A = (Q/M_T)(M_T/A) = (Q/V)L_E$, where Q/M_T is the total-mass-normalized specific capacity, M_T/A is the total electrode mass loading (including additives), Q/V is the volumetric capacity and L_E is the electrode thickness. The two different specific capacities are related by $Q/M_T = f_{Act} \times Q/M_{Act}$, where f_{Act} is the fraction of active mass within the electrode. In addition, $Q/V = \rho_E \times Q/M_T$ where ρ_E is the electrode mass density. Thus, to maximize the areal capacity, it is necessary to maximize the amount of active material within the electrode which can be done by maximizing f_{Act} and L_E (i.e., M_T/A).[16,29d,30,34a]

In our electrodes, f_{Act} is 80% which is reasonably high. However, incorporating 20 wt.% SWCNT in our electrodes has two important additional benefits as mentioned above: it enhances mechanical robustness[29d,34a,16] and electrical conductivity.[31,34b] These enhancements are particularly important for thick electrodes.

So far, we have examined thin (M_T/A = 0.56 mg cm^{-2}, ≈7 µm thick), KFC-based electrodes to determine their optimal performance. However, commercial battery electrodes are usually much thicker, possibly up to 100 microns. In order to fully explore the potential of our electrodes, we fabricated KFC/SWCNT nanoplatelet electrodes at seven different mass loadings (M_T/A between 0.38 and 9.5 mg cm^{-2}) for

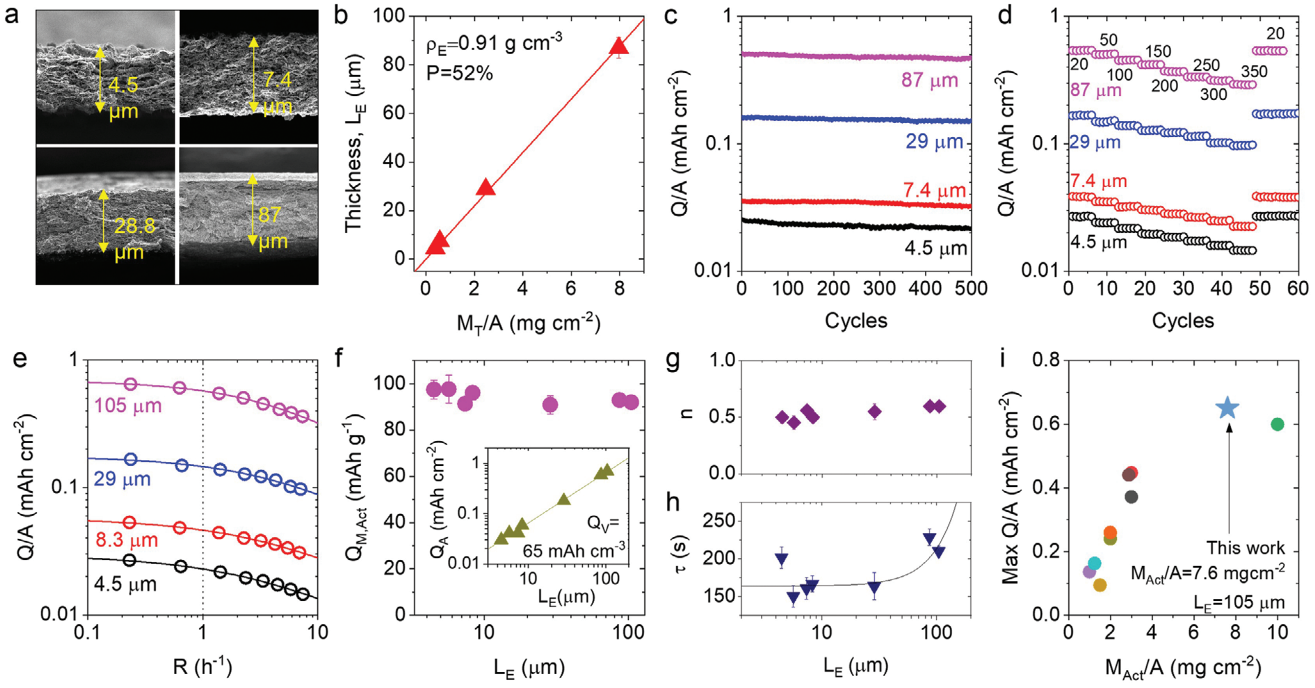

Figure 4. Performance of KFC/SWCNT cells at various electrode thicknesses (L_E). a) SEM images of cross sections of four electrodes with average thickness values as shown in the panel. b) Measured thickness as a function of the total electrode mass density (M_T/A, i.e., including both nanotubes and active material). The electrode density and porosity extracted from the linear fit are shown in the panel. c) Areal capacity (Q/A) measured for 500 cycles at a current density of 50 mA g^{-1} for the four electrodes shown in (a). d) Capacity of electrodes shown in a plotted as a function of cycle number, measured at different current densities as indicated on the panel in units of mA g^{-1}. e) Areal capacity for four electrodes of various thicknesses plotted as a function of rate, R ($R = I/Q$). The lines are fits to Equation (2). f–h) Parameters extracted from the fits in e for all seven electrodes studied. f) inset, shows Q_A (the areal capacity at very low rate) plotted versus electrode thickness. The straight line is consistent with a low-rate volumetric capacity of 65 mAh cm^{-2}. f) main plot shows $Q_{M,Act}$ (the active-ass-normalized capacity at very low rate) as calculated from Q_A. g) and h) show the n and τ parameters plotted versus electrode thickness. In (h) the line is a fit to Equation (3). i) Measured areal capacity (at lowest applied current) for this work is (star) compared to various literature values (see Table S2, Supporting Information).

electrochemical characterization. To measure the thickness of the electrodes via cross-sectional SEM imaging, we selected four electrodes with M_T/A = 0.39, 0.56, 2.5, and 8 mg cm^{-2} (**Figure** 4a). The resultant mean measured electrode thicknesses (L_E) were 4.5, 7.4, 28.8, and 87 μm, respectively. The mean electrode thicknesses are plotted versus the total mass loading in Figure 4b. Good linearity is observed in line with the expected relationship: $M_T/A = \rho_E L_E$. From the slope, we find the electrode density, $\rho_E = 0.91 \pm 0.03$ g cm^{-3}. This density was then combined with M_T/A to find the thicknesses of the other three electrodes, giving an overall thickness range of 4.5–105 μm for our electrodes. The measured electrode density implies an electrode porosity of 52 ± 2%. Thus, there is a significant pore volume which will allow electrolytes to enter the electrode, facilitating ion transport to the surface of all $K_3Fe(CN)_6$ nanoplatelets. This porosity value falls within the range of 50–60% observed in previous studies on nanosheet/nanotube composites.[26a,29d,38a,47]

We then performed galvanostatic charge–discharge measurements as a function of cycle number, both at constant current and while varying the current for electrodes with all thicknesses (Figure S9, Supporting Information), and found voltage profiles very similar to those in Figure 3c in all cases (for 105 μm electrodes, see Figure S10, Supporting Information). Figure 4c shows the resultant areal capacity (Q/A), measured over 500 cycles @ 50 mA g^{-1} for the four electrodes with measured thicknesses. The areal capacities are very stable. For example, for the thickest electrode (for 105 μm electrodes), the capacity decays by <10% over 500 cycles (Figure S10, Supporting Information). Rate performance measurements were made for all seven electrodes at current densities between 20 and 350 mA g^{-1}, with a subset of data shown in Figure 4d. In all cases, only modest reductions in areal capacity are found with increasing current. In addition, for each electrode, once the current was returned to its lowest value, the areal capacity also reverted to very close to its initial value. Notably, 2D-KFC/SWCNT has achieved a remarkable areal capacity along with impressive cycling stability of over 500 cycles with 92 ± 2% retention in the specific capacity (Figure S11, Supporting Information).

It is important to mention that experiments using large-area electrodes (A = 1.13 cm^2, Figure S12, Supporting Information) offer consistent cycling performance compared to electrodes with an area of 0.178 cm^2, which is likely a result of the development of a strong electrode architecture with chemical durability. Furthermore, the direct use of bulk-KFC as a K-ion cathode demonstrates inferior performance compared to the 2D-KFC/SWCNTs composite electrode (Figure S13, Supporting Information).

2.4. Quantitative Analysis of Rate Data

It is possible to perform a more quantitative analysis on the rate performance data.[31,32,34b,48] To do this, the data is plotted as capacity (in this case areal capacity) versus a rate parameter, R [units h^{-1} or s^{-1}], which we define as the charge/discharge current, I [units mA], divided by the measured capacity, Q [units mAh], measured at that current, that is, R = I/Q.[31,48b] In practice, this is calculated via $R = (I/M_{Act})/(Q/M_{Act})$ or $R = (I/A)/(Q/A)$. As shown in Figure 4e, we plot Q/A versus R for electrodes of four different thicknesses, including our thickest electrode ($L_E = 105$ µm). In all cases, we see plateau-like behavior for low R with the areal capacity falling off at higher R as expected.[31]

One important point is that the capacities at the lowest rate ($R \approx 0.25\ h^{-1}$) varied from 0.027 mAh cm^{-2} for the thinnest electrode to 0.65 mAh cm^{-2} for the thickest (all at 20 mA g^{-1}). As we shall see below, the latter value is high compared to reported results for the family of PBAs. It is worth noting that the R-value is the inverse of the charging time. Thus, the vertical dotted line in Figure 4e indicates a charging time of 1 h. This data shows that our thickest electrode can be charged up to 0.6 mAh cm^{-2} in 1 h. This emphasizes the excellent rate performance of our electrodes.

Data such as that in Figure 4e can be fit using the following semi-empirical equation:[31]

$$\frac{Q}{A} = Q_A \left[1 - (R\tau)^n \left(1 - e^{-(R\tau)^{-n}}\right)\right] \tag{2}$$

This equation has three fit parameters: Q_A, τ and n. Q_A is the areal capacity at an extremely low rate, that is, $Q_A = \lim_{R \to 0}(Q/A)$. This can be considered the maximum accessible areal capacity for the electrode under study. τ is the characteristic time associated with the charge–discharge process and is related to the R-value above which the capacity starts to fall off.[31] Finally, n is a parameter which describes how fast the capacity fades at high rates. Values of $n \approx 0.5$ are found for electrodes which are diffusion limited whereas values near 1 denote electrically (i.e., capacitance) limited systems.[31]

This equation has been fit to the experimental data as shown (solid lines) in Figure 4e. In all cases, excellent fits are found. The resultant low-rate areal capacities, Q_A, are plotted versus L_E in Figure 4f (inset). The maximum value of Q_A for the $L_E = 105$ µm electrode was 0.75 mAh cm^{-2} (N.B. this value is an extrapolation of the areal capacity measured at zero current). That the data follows a straight line ($Q_A = Q_V L_E$, expressing all capacities by their low-rate values) shows that all of the electrode volume is electrochemically active. From the slope of this line, we extract an average low-rate volumetric capacity of $\langle Q_V \rangle = 65$ mAh cm^{-3}.

We can use there are Q_A values to calculate the low-rate, active-mass-normalized specific capacity, $Q_{M,Act}$, via $Q_A = L_E \times \rho_E \times f_{Act} \times Q_{M,Act}$. The resultant values are plotted versus L_E in Figure 4f. We find no significant decay with electrode thickness with values between 91 and 98 mAh g^{-1}. This value can be compared with the theoretical capacity of 81 mAh g^{-1} for $K_3Fe(CN)_6$. We believe that the extra storage capacity beyond theoretical capacity can be attributed to two key factors. First, the capacity gain likely arises from ion storage facilitated by the nanotubes, as illustrated in Figure S7c (Supporting Information). Furthermore, the exfoliation process of non-layered materials is expected to generate amorphous nanoplatelets, which may enhance porosity and internal surface area, thereby adding extra capacity. This data shows that our strategy of producing nanoplatelets and mixing them with SWCNT allows us to realize all of the theoretical capacity.

The n parameter is plotted versus L_E in Figure 4g and displays values very close to 0.5 over the whole thickness range. This is important as it indicates that these electrodes are limited almost completely by ion diffusion at all thicknesses. This means that the rate-limiting factor is a combination of liquid-phase diffusion of ions within the electrolyte in the pores of the electrode and solid-state diffusion of K^+ ions within the $K_3Fe(CN)_6$ nanoplatelets.[31]

The characteristic time associated with charge/discharge, τ, is plotted versus L_E in Figure 4h. This parameter shows values between 150 and 230 s increasing slightly with electrode thickness. This is interesting for a number of reasons. First, the relatively weak thickness dependence of τ casts light on the rate-limiting mechanisms. By now, it is well known that τ depends on L_E in a well-defined way.[31,32] A physical model has been proposed that defines contributions to τ from various physical processes which can be divided into diffusive and electrical (capacitive) effects.[31,32] From the data in Figure 4g, it is clear that diffusive effects are dominant here. The two main diffusive effects, solid-state diffusion and in-pore liquid diffusion depend differently on electrode thickness. Solid state diffusion occurs on a timescale which is independent of the electrode thickness but instead depends on the particle size. In contrast, liquid-phase diffusion in the pores of the electrode occurs on a timescale which increases quadratically with L_E.[31] We can make a crude approximation that only these two effects make a significant contribution to τ in this case. Then, using only these terms from the more general model,[31] we can express τ as:

$$\tau = \frac{L_E^2}{D_{BL} P_E^{3/2}} + \frac{L_{AM}^2}{D_{AM}} \tag{3}$$

here, D_{BL} is the diffusion coefficient of K^+ ions in the electrolyte, D_{AM} is the solid-state diffusion coefficient of K^+ ions in KFC and L_{AM} is the solid-state diffusion length in KFC. We know $P_E = 52 \pm 2\%$ from above and approximate L_{AM} as half the mean nanoplatelet thickness ($L_{AM} \le t > /2 = 11 \pm 1$ nm). These very short diffusion paths are possible because, unlike layered 2D materials, these platelets can support diffusion perpendicular to the plane of the platelet. We can fit the data in Figure 4h using Equation (3), obtaining good agreement. From the fit parameters, and using the values quoted above, we obtain $D_{BL} = 5.6 \pm 1.8 \times 10^{-10}\ m^2\ s^{-1}$. This is close to the value of $D_{BL} = 5.5 \times 10^{-10}\ m^2\ s^{-1}$ for K ions in 2 M KFSI-DME reported in ref.[49] However, we note that the apparent close agreement may be slightly fortuitous given the simplicity of our model and the limited number of electrode thicknesses in our study. In addition we find $D_{AM} = 7.4 \pm 2 \times 10^{-19}\ m^2\ s^{-1}$ which is similar to the reported diffusivity of K^+ ions in carbon-coated $K_4Fe(CN)_6$ ($10^{-18}\ m^2\ s^{-1}$).[50] We note that our D_{AM} value is very small, compared to the broad cohort of 2D materials as a whole,[48c] despite the open structure of KFC. Nevertheless, the small diffusion lengths (≈11 nm) of our KFC nanoplatelets yield small solid-state diffusion times, so slow diffusion does not necessarily hinder rate performance in a practical sense.

Previously, we have argued that the rate performance of battery electrodes can be characterized by a figure of merit: L_E^2/τ, with larger values representing better rate performance.[31,48c] By analyzing the data in a large number of papers, we found that lithium and sodium storing electrodes based on 2D materials tend to display values of L_E^2/τ between 10^{-14} and 10^{-10} $\text{m}^2\ \text{s}^{-1}$.[48c] The thickest electrode under study here displayed $L_E^2/\tau = 4 \times 10^{-11}$ $\text{m}^2\ \text{s}^{-1}$, very close to the upper limit of this range. This shows that our KFC-based electrodes display state-of-the-art rate behavior within the family of 2D-based electrodes. As mentioned above, this is largely due to their low thickness and hence small solid-state diffusion lengths. An additional factor is that the low aspect ratio of our nanoplatelets ($<L/t \geq 5$) means that the tortuosity of the electrolyte-filled pore system within the electrode is low.[48c] This leads to relatively fast diffusion of the K^+ ions within the pore system reducing liquid-diffusion as a potential rate-limiting step.[31,48c]

This analysis shows that the rate performance of KFC electrodes is consistent with theoretical expectations for heavily diffusion-limited systems. While the thickest electrodes show a significant contribution from diffusion in the electrolyte, the thinner electrodes are almost exclusively limited by solid-state diffusion. The relatively low solid-state diffusivity highlights the importance of engineering ultra-short diffusion paths and hence the need for very thin KFC platelets. This vindicates our approach of producing a 2D form of KFC.

Finally, we compare the low-rate areal capacities of our electrodes to best-performing PBAs in the literature. Table S2 (Supporting Information) presents a comprehensive comparison of the specific and measured areal capacities achieved by our KFC/SWCNT cathodes with the best-performing Prussian blue analogs. The electrochemical performance of our KFC/SWCNT cathodes is graphically compared to the best literature values in Figure 4i, where the maximum measured areal capacity is plotted against active material mass loading. The areal capacity of our KFC/SWCNT cathodes exceeds the best-reported values for all of the highest-performing K-ion storing electrodes fabricated using Prussian blue analogs. These findings emphasize the huge potential of our cathodes which were produced using cheap, commercially available KFC.

Finally, we note that although this work is promising, barriers remain before KFC can be directly used as a cathode material. The main problem is that this material has no electrochemically active potassium. This means it cannot be combined with a K-deficient anode material unless it is pre-potassiated. However, we note that a similar problem has been resolved for some K-poor Prussian blue analogs. A number of papers have shown that full-cells can be made by combining the K-poor cathode with a pre-potassiated anode before the assembly of the full cell. The full cell can then be activated by a pre-discharge process.[51]

3. Conclusion

In this paper, we investigated the use of commercially available potassium ferricyanide as a cost-effective and easily processable cathode material for potassium-ion batteries. We employed a simple liquid-phase exfoliation process to create nanoplatelets of 2D KFC. These nanoplatelets were determined to be amorphous, with a quasi-2D morphology and an aspect ratio of 5. TEM-EDX analysis confirmed the stoichiometry of these nanoplatelets. Stable electrodes were fabricated by combining these KFC nanoplatelets with carbon nanotubes and subjecting them to a vacuum filtration process. The composite electrodes of KFC/SWCNT exhibited exceptional capacity and promising rate performance as a cathode for use in KIBs. Specifically, a reversible capacity of 80 mAh g^{-1} at 50 mA g^{-1} and maintained 91.5% capacity retention after 500 cycles. Increasing the mass loadings of KFC allowed for the production of thick electrodes up to 105 microns in thickness, capable of storing ≈0.65 mAh cm^{-2} capacity at a current density of 20 mA g^{-1}. Detailed rate analysis indicated that the thickest electrodes demonstrate a notable contribution from diffusion in the electrolyte. In contrast, the thinner electrodes are primarily restricted by solid-state diffusion. Nonetheless, our thickest electrodes exhibited state-of-the-art rate performance because of the combination of low platelet thickness and aspect ratio. The importance of engineering ultra-short diffusion paths and the need for very thin KFC platelets is underscored by our electrodes' relatively low solid-state diffusivity. We believe that this study illustrates the potential of utilizing commercial KFC as a promising cathode material for KIBs, thereby facilitating the development of cost-effective and high-performance energy storage solutions.

4. Experimental Section

Synthesis of $K_3Fe(CN)_6$ Nanoplatelets: The $K_3Fe(CN)_6$ crystals were sourced commercially (Sigma-Aldrich, product number-455946, 99.98% purity). This powder (800 mg) was bath-sonicated in a dried, distilled, and de-gassed 40 mL of 2-propanol solvent in an inert argon-gas atmosphere for 10 h. The initial starting concentration was kept at 20 mg ml^{-1}. A round-bottom flask was used in the sonication process (Branson ultrasonic bath, CPX2800-E, 130 W). The dispersion was cooled periodically by exchanging the bath water with ice-cooled water every 30 min to maintain a temperature <10 °C. Following sonication, the obtained dispersion underwent two consecutive centrifugation steps. The first step involved centrifugation at 100 g for 2 h aimed at removing large and thick unexfoliated particles. The supernatant obtained after this step was separated from sediment under the inert atmosphere and subjected to a second centrifugation step at 3800 g for 2 h. This step ensured the removal of impurities and defective nanomaterial that typically present in the supernatant at higher speeds, leaving pristine nanoplatelets in the sediment. The sediment was then redispersed in fresh 2-propanol solvent (10 mL), and the concentration was carefully measured via filtering resulting in 10–12 mg ml^{-1} concentration. The mass of exfoliated material obtained in a single batch of exfoliation is 100–120 mg. The yield was calculated to be 13–15% with a production output of 12 mg ml^{-1} h. This resultant material was used for characterization, and for the formation of the nanocomposite electrode.

Electrode Formation: In the first step, a dispersion of SWCNT was prepared in 2-propanol with the goal of achieving a concentration of <0.1 mg ml^{-1} to prevent nanotube aggregation in the obtained dispersion. To achieve this, 8 mg of P3-SWCNT was suspended in 80 ml of 2-propanol, and the resulting solution underwent probe sonication for 3 h using a horn-tip sonic probe (Vibracell CVX, 750 W). The amplitude was set at 50% with a pulse duration of 6 s on/2s off. The temperature was carefully maintained at <10 °C throughout the probe sonication process by employing ice-cooling. The outcome of this process was a black dispersion, which was allowed to free-stand for 2 h. Afterward, the top two-thirds of the dispersion were separated, and its final concentration was measured via filtering, resulting in a concentration of 0.085 mg ml^{-1}. In the second step, the exfoliated dispersion of $K_3Fe(CN)_6$ was mixed with the SWCNT dispersion in the weight ratio of 80:20 and was bath sonicated for 30 min to ensure uniform mixing. In the final step, the resultant mixture was vacuum filtered using Celgard 2320 membrane with a thickness, 20 µm and area of 2 cm^2. This resulted in a free-standing nanocomposite film that would be utilized as an electrode. The resulting film was then sectioned into an area of 0.178 cm^2 at seven different mass loadings (M_T/A values of 0.38, 0.53, 0.56, 0.76, 2.47, 7.96, and 9.54 mg cm^{-2}) for electrochemical testing. The SEM cross-sectional measurements were used to determine the thickness of four electrodes, which had areal mass-loadings (M_T/A) of 0.38 mg cm^{-2}, 0.56 mg cm^{-2}, 2.45 mg cm^{-2}, and 8 mg cm^{-2}, resulting in thickness values of 4.5, 7.4, 28.8, and 87 µm, respectively. The density of the electrodes was determined by plotting mass loading versus electrode thickness. This density was then used with M_T/A to calculate the thicknesses of the remaining three electrodes (yielding 5.7, 8.3, 105 µm), leading to an overall thickness range of 4.5–105 µm for all the electrodes.

Assembly of K-Ion Half-Cell: K-ion half cells were assembled using CR-2032 type coin cells (14 mm; MTI Corp.) in a glovebox filled with argon, ensuring O_2 and H_2O levels were maintained below 0.1 ppm. Potassium metal pieces, initially soaked in mineral oil within the glovebox, were wiped clean to remove the oil. Subsequently, the metal pieces were cut and sliced with a blade to expose fresh metal surfaces and then rolled into flat discs for use as counter/reference electrodes. Whatman glass fiber filters (GD/D, diameter 90 mm) were employed as separators, and aluminum foil was used as a current collector. The electrolyte consisted of potassium bis(fluorosulfonyl)imide (KFSI, 2 M) dissolved in triethyl phosphate (TEP). After assembly within the glove box, the cells were removed and placed in an oven at 40 °C for 24 h before conducting electrochemical measurements.

Characterization: The UV–vis extinction and absorption measurements were conducted using a Perkin Elmer Lambda 1050 spectrometer within the wavelength range of 250 to 800 nm. Quartz cuvettes with a 4 mm pathlength were employed for this purpose. The concentration of the dispersion was determined by filtering and weighing membranes (Celgard 2320) to calculate the extinction coefficient spectra. For absorbance spectra, a setup utilizing an integration sphere with a radius of 150 mm was employed. Transmission electron microscopy (TEM) imaging was performed using a JEOL 2100 instrument on holey carbon grids (400 mesh) with an accelerating voltage of 200 KV. X-ray diffraction (XRD) spectra were obtained with a Bruker D8 Discover high-resolution diffractometer equipped with a copper tube emitting K_α radiation (wavelength of 1.5406 Å) and a double-bounce Ge [220] monochromator. The spectra were acquired in the 2θ range from 10 to 80 on films prepared on silicon (100) wafers, and on electrodes. For Raman spectroscopy, inks of exfoliated $K_3Fe(CN)_6$ were drop cast onto Si/SiO_2 substrate and annealed at 120 °C. The bulk powder was placed on a Si/SiO_2 substrate. A WITec Raman spectrometer at 532 nm with a 20× objective was used to acquire spectra. Each spectrum was averaged over 3 accumulations. An incident power of ≈1 mW to minimize possible thermal damage. Atomic force microscopy (AFM) was carried out using a Bruker multimode 8 microscope in ScanAsyst mode, employing an OLTESPA R3 cantilever. The samples for AFM were prepared by drop-casting a diluted dispersion on silicon wafers and heating it at 80 °C, followed by drying using argon gas. Scanning electron microscopy (SEM) was performed using a Carl ZEISS Ultra Plus SEM. Samples were mounted on aluminum SEM stubs using conductive carbon tabs (Ted Pella) and grounded using conductive silver paint (PELCO, Ted Pella). All images were captured at an accelerating voltage of 2 kV using a working distance of 5 mm and a 30 µm aperture. Both the Inlens and SE2 detectors were used for imaging. The stoichiometry and detailed elemental compositions of bulk and 2D-form of KFC were calculated using SEM-EDX results. Cross-sectional SEM images of battery electrodes were taken by fracturing the free-standing electrodes. The average electrode thickness was determined by measuring the thickness from SEM cross-sections across the electrode.

Supporting Information

Supporting Information is available from the Wiley Online Library or from the author.

Acknowledgements

The authors acknowledge the Graphene Flagship and the Science Foundation Ireland (SFI) funded center AMBER (SFI/12/RC/2278_P2) and have availed of the facilities of the SFI-funded advanced microscopy laboratory (AML). B.K. acknowledges research funding from the Science Foundation Ireland (SFI)-IRC pathway program (grant number 22/PATH-S/10706). C.G. acknowledges research supported by the European Union through the Horizon Europe project 2D-PRINTABLE (GA-101135196).

Conflict of Interest

The authors declare no conflict of interest.

Data Availability Statement

The data that support the findings of this study are available in the supplementary material of this article.

Keywords

2D Potassium ferricyanide, areal capacities, potassium-ion batteries, prussian blue analogs, rate performance

Received: January 23, 2025
Published online:

---

[1] J. B. Goodenough, K.-S. Park, *J. Am. Chem. Soc.* **2013**, *135*, 1167.
[2] a) T. Wulandari, D. Fawcett, S. B. Majumder, G. E. J. Poinern, *Battery Energy* **2023**, *2*, 20230030; b) J. M. Tarascon, M. Armand, *Nature* **2001**, *414*, 359.
[3] a) K. Kubota, M. Dahbi, T. Hosaka, S. Kumakura, S. Komaba, *Chem. Rec.* **2018**, *18*, 459; b) T. Hosaka, K. Kubota, A. S. Hameed, S. Komaba, *Chem. Rev.* **2020**, *120*, 6358.
[4] a) J. Deng, W.-B. Luo, S.-L. Chou, H.-K. Liu, S.-X. Dou, *Adv. Energy Mater.* **2018**, *8*, 1701428; b) Y.-S. Hu, Y. Li, *ACS Energy Lett.* **2021**, *6*, 4115.
[5] X. Min, J. Xiao, M. Fang, W. Wang, Y. Zhao, Y. Liu, A. M. Abdelkader, K. Xi, R. V. Kumar, Z. Huang, *Energy Environ. Sci.* **2021**, *14*, 2186.
[6] Y. Xu, M. Titirici, J. Chen, F. Cora, P. L. Cullen, J. S. Edge, K. Fan, L. Fan, J. Feng, T. Hosaka, J. Hu, W. Huang, T. I. Hyde, S. Imtiaz, F. Kang, T. Kennedy, E. J. Kim, S. Komaba, L. Lander, P. N. Le Pham, P. Liu, B. Lu, F. Meng, D. Mitlin, L. Monconduit, R. G. Palgrave, L. Qin, K. M. Ryan, G. Sankar, D. O. Scanlon, et al., *J. Phys.: Energy* **2023**, *5*, 021502.
[7] W. Zhang, Y. Liu, Z. Guo, *Sci. Adv.* **2019**, *5*, eaav7412.
[8] a) L. Fan, R. Ma, Q. Zhang, X. Jia, B. Lu, *Angew. Chem.* **2019**, *131*, 10610; b) J. Yu, M. Jiang, W. Zhang, G. Li, R. A. Soomro, N. Sun, B. Xu, *Small Methods* **2023**, *7*, 2300708.
[9] Y. Ding, X. Guo, Y. Qian, L. Zhang, L. Xue, J. B. Goodenough, G. Yu, *Adv. Mater.* **2019**, *31*, 1806956.
[10] S. Liu, L. Kang, S. C. Jun, *Adv. Mater.* **2021**, *33*, 2004689.

[11] S. Zhao, Z. Guo, K. Yan, X. Guo, S. Wan, F. He, B. Sun, G. Wang, *Small Struct.* **2021**, *2*, 2000054.

[12] S. Kjeldgaard, I. Dugulan, A. Mamakhel, M. Wagemaker, B. B. Iversen, A. Bentien, *R. Soc. Open Sci.* **2021**, *8*, 201779.

[13] C. D. Wessells, R. A. Huggins, Y. Cui, *Nat. Commun.* **2011**, *2*, 550.

[14] a) X. H. Liu, J. Peng, W. H. Lai, Y. Gao, H. Zhang, L. Li, Y. Qiao, S. L. Chou, *Adv. Funct. Mater.* **2022**, *32*, 2108616; b) J. Qian, C. Wu, Y. Cao, Z. Ma, Y. Huang, X. Ai, H. Yang, *Adv. Energy Mater.* **2018**, *8*, 1702619.

[15] a) P. Zhu, P. R. Slater, E. Kendrick, *Mater. Des.* **2022**, *223*, 111208; b) A. Etiemble, N. Besnard, A. Bonnin, J. Adrien, T. Douillard, P. Tran-Van, L. Gautier, J. C. Badot, E. Maire, B. Lestriez, *J. Mater. Sci.* **2017**, *52*, 3576.

[16] S.-H. Park, P. J. King, R. Tian, C. S. Boland, J. Coelho, C. Zhang, P. McBean, N. McEvoy, M. P. Kremer, D. Daly, J. N. Coleman, V. Nicolosi, *Nat. Energy* **2019**, *4*, 560.

[17] D. Gao, R. Du, C. Zhou, B. Han, K. Xia, Q. Gao, J. Wu, *Mater. Today Energy* **2018**, *10*, 302.

[18] K. J. Nelson, I. D. Giles, W. W. Shum, A. M. Arif, J. S. Miller, *Angew. Chem., Int. Ed.* **2005**, *44*, 3129.

[19] B. Figgis, B. Skelton, A. White, *Aust. J. Chem.* **1978**, *31*, 1195.

[20] a) J. N. Coleman, M. Lotya, A. O'Neill, S. D. Bergin, P. J. King, U. Khan, K. Young, A. Gaucher, S. De, R. J. Smith, I. V. Shvets, S. K. Arora, G. Stanton, H. Y. Kim, K. Lee, G. T. Kim, G. S. Duesberg, T. Hallam, J. J. Boland, J. J. Wang, J. F. Donegan, J. C. Grunlan, G. Moriarty, A. Shmeliov, R. J. Nicholls, J. M. Perkins, E. M. Grieveson, K. Theuwissen, D. W. McComb, P. D. Nellist, et al., *Science* **2011**, *331*, 568; b) C. Backes, D. Campi, B. M. Szydlowska, K. Synnatschke, E. Ojala, F. Rashvand, A. Harvey, A. Griffin, Z. Sofer, N. Marzari, J. N. Coleman, D. D. O'Regan, *ACS Nano* **2019**, *13*, 7050.

[21] H. Kaur, J. N. Coleman, *Adv. Mater.* **2022**, *34*, 2202164.

[22] C. S. Naiman, *J. Chem. Phys.* **1961**, *35*, 323.

[23] A. Saito, Y. Morioka, I. Nakagawa, *J. Phys. Chem.* **1984**, *88*, 480.

[24] M. M. Barsan, I. S. Butler, J. Fitzpatrick, D. F. R. Gilson, *J. Raman Spectrosc.* **2011**, *42*, 1820.

[25] a) C. Backes, T. M. Higgins, A. Kelly, C. Boland, A. Harvey, D. Hanlon, J. N. Coleman, *Chem. Mater.* **2017**, *29*, 243; b) V. Nicolosi, M. Chhowalla, M. G. Kanatzidis, M. S. Strano, J. N. Coleman, *Science* **2013**, *340*, 1226419.

[26] a) H. Kaur, R. Tian, A. Roy, M. McCrystall, D. V. Horvath, G. Lozano Onrubia, R. Smith, M. Ruether, A. Griffin, C. Backes, V. Nicolosi, J. N. Coleman, *ACS Nano* **2020**, *14*, 13418; b) G. Guan, J. Xia, S. Liu, Y. Cheng, S. Bai, S. Y. Tee, Y.-W. Zhang, M.-Y. Han, *Adv. Mater.* **2017**, *29*, 1700326.

[27] T. Chen, H. Kaur, M. McCrystall, R. Tian, A. Roy, R. Smith, D. V. Horvath, J. Maughan, B. Konkena, M. Venkatesan, K. Synnatschke, T. Carey, J. Liu, J. Pepper, R. Zhang, C. Backes, V. Nicolosi, H. Xia, J. N. Coleman, *FlatChem* **2022**, *33*, 100360.

[28] K. R. Paton, E. Varrla, C. Backes, R. J. Smith, U. Khan, A. O'Neill, C. Boland, M. Lotya, O. M. Istrate, P. King, T. Higgins, S. Barwich, P. May, P. Puczkarski, I. Ahmed, M. Moebius, H. Pettersson, E. Long, J. Coelho, S. E. O'Brien, E. K. McGuire, B. M. Sanchez, G. S. Duesberg, N. McEvoy, T. J. Pennycook, C. Downing, A. Crossley, V. Nicolosi, J. N. Coleman, *Nat. Mater.* **2014**, *13*, 624.

[29] a) X. Zang, T. Wang, Z. Han, L. Li, X. Wu, *Nano* **2019**, *14*, 1930001; b) C. Zhang, H. Pan, L. Sun, F. Xu, Y. Ouyang, F. Rosei, *Energy Storage Mater.* **2021**, *38*, 354; c) Q. Yun, L. Li, Z. Hu, Q. Lu, B. Chen, H. Zhang, *Adv. Mater.* **2020**, *32*, 1903826; d) H. Kaur, B. Konkena, C. Gabbett, R. Smith, M. McCrystall, R. Tian, A. Roy, T. Carey, V. Vega-Mayoral, V. Nicolosi, J. N. Coleman, *Adv. Energy Mater.* **2023**, *13*, 2203013.

[30] Y. Chen, B. Zhao, Y. Yang, A. Cao, *Adv. Energy Mater.* **2022**, *12*, 2201834.

[31] R. Tian, S.-H. Park, P. J. King, G. Cunningham, J. Coelho, V. Nicolosi, J. N. Coleman, *Nat. Commun.* **2019**, *10*, 1933.

[32] D. V. Horváth, J. Coelho, R. Tian, V. Nicolosi, J. N. Coleman, *ACS Appl. Energy Mater.* **2020**, *3*, 10154.

[33] a) R. C. Chiu, T. J. Garino, M. J. Cima, *J. Am. Ceram. Soc.* **1993**, *76*, 2257; b) K. B. Singh, M. S. Tirumkudulu, *Phys. Rev. Lett.* **2007**, *98*, 218302.

[34] a) R. Tian, A. Griffin, M. McCrystall, M. Breshears, A. Harvey, C. Gabbett, D. V. Horváth, C. Backes, Y. Jing, T. Heine, S.-H. Park, J. Coelho, V. Nicolosi, M. Nentwig, C. Benndorf, O. Oeckler, J. N. Coleman, *Adv. Energy Mater.* **2021**, *11*, 2002364; b) R. Tian, N. Alcala, S. J. K. O'Neill, D. V. Horvath, J. Coelho, A. J. Griffin, Y. Zhang, V. Nicolosi, C. O'Dwyer, J. N. Coleman, *ACS Appl. Energy Mater.* **2020**, *3*, 2966.

[35] S. Zhu, J. Ni, *Chem. Rec.* **2022**, *22*, 202200125.

[36] a) C. Gabbett, C. S. Boland, A. Harvey, V. Vega-Mayoral, R. J. Young, J. N. Coleman, *Chem. Mater.* **2018**, *30*, 5245; b) Y. Liu, X. He, D. Hanlon, A. Harvey, U. Khan, Y. Li, J. N. Coleman, *ACS Nano* **2016**, *10*, 5980.

[37] X. Wu, W. Deng, J. Qian, Y. Cao, X. Ai, H. Yang, *J. Mater. Chem. A* **2013**, *1*, 10130.

[38] a) H. Kaur, B. Konkena, M. McCrystall, K. Synnatschke, C. Gabbett, J. Munuera, R. Smith, Y. Jiang, R. Bekarevich, L. Jones, V. Nicolosi, J. N. Coleman, *ACS Nano* **2024**, *18*, 20213; b) M. R. Palacín, *Chem. Soc. Rev.* **2009**, *38*, 2565.

[39] M. S. Palagonia, C. Erinmwingbovo, D. Brogioli, F. L. Mantia, *J. Electroanal. Chem.* **2019**, *847*, 113170.

[40] B. Konkena, C. Kalapu, H. Kaur, A. Holzinger, H. Geaney, V. Nicolosi, M. D. Scanlon, J. N. Coleman, *ACS Appl. Mater. Interfaces* **2023**, *15*, 58320.

[41] a) C. Zhang, Y. Xu, M. Zhou, L. Liang, H. Dong, M. Wu, Y. Yang, Y. Lei, *Adv. Funct. Mater.* **2017**, *27*, 1604307; b) X. Jiang, T. Zhang, L. Yang, G. Li, J. Y. Lee, *ChemElectroChem* **2017**, *4*, 2237.

[42] S. Chong, Y. Chen, Y. Zheng, Q. Tan, C. Shu, Y. Liu, Z. Guo, *J. Mater. Chem. A* **2017**, *5*, 22465.

[43] a) J. Qian, M. Zhou, Y. Cao, X. Ai, H. Yang, *Adv. Energy Mater.* **2012**, *2*, 410; b) M. Qin, W. Ren, J. Meng, X. Wang, X. Yao, Y. Ke, Q. Li, L. Mai, *ACS Sustainable Chem. Eng.* **2019**, *7*, 11564.

[44] Y. Xu, T. Ding, D. Sun, X. Ji, X. Zhou, *Adv. Funct. Mater.* **2023**, *33*, 2211290.

[45] S. Liu, J. Mao, Q. Zhang, Z. Wang, W. K. Pang, L. Zhang, A. Du, V. Sencadas, W. Zhang, Z. Guo, *Angew. Chem., Int. Ed.* **2020**, *59*, 3638.

[46] J. Liao, Q. Hu, Y. Yu, H. Wang, Z. Tang, Z. Wen, C. Chen, *J. Mater. Chem. A* **2017**, *5*, 19017.

[47] B. Konkena, H. Kaur, R. Tian, C. Gabbett, M. McCrystall, D. V. Horvath, K. Synnatschke, A. Roy, R. Smith, V. Nicolosi, M. D. Scanlon, J. N. Coleman, *Small* **2022**, *18*, 2203918.

[48] a) D. V. Horváth, R. Tian, C. Gabbett, V. Nicolosi, J. N. Coleman, *J. Electrochem. Soc.* **2022**, *169*, 030503; b) S.-H. Park, R. Tian, J. Coelho, V. Nicolosi, J. N. Coleman, *Adv. Energy Mater.* **2019**, *9*, 1901359; c) R. Tian, M. Breshears, D. V. Horvath, J. N. Coleman, *ACS Nano* **2020**, *14*, 3129.

[49] S. Dhir, B. Jagger, A. Maguire, M. Pasta, *Nat. Commun.* **2023**, *14*, 3833.

[50] Y. Pei, C. Mu, H. Li, F. Li, J. Chen, *ChemSusChem* **2018**, *11*, 1285.

[51] a) X. L. Lu, Z. Liang, Z. Fang, D. D. Zhang, Y. P. Zheng, Q. Liu, D. F. Fu, J. Teng, W. Y. Yang, *Carbon Energy* **2024**, *6*, e490; b) Q. W. Zhou, H. K. Liu, S. X. Dou, S. K. Chong, *ACS Nano* **2024**, *18*, 7287; c) Y. H. Zhu, X. Yang, D. Bao, X. F. Bie, T. Sun, S. Wang, Y. S. Jiang, X. B. Zhang, J. M. Yan, Q. Jiang, *Joule* **2018**, *2*, 736.